Journal of Neuroscience Methods 181 (2009) 268–282

Contents lists available at ScienceDirect

Journal of Neuroscience Methods

journal homepage: www.elsevier.com/locate/jneumeth

# A Mathematical Model for Understanding the STatistical effects of *k*-space (AMMUST-k) preprocessing on observed voxel measurements in fcMRI and fMRI

Andrew S. Nencka [a], Andrew D. Hahn [a], Daniel B. Rowe [a,b,*]

[a] Department of Biophysics, Medical College of Wisconsin, Milwaukee, WI, USA
[b] Division of Biostatistics, Medical College of Wisconsin, Milwaukee, WI, USA

ARTICLE INFO

*Article history:*
Received 23 March 2009
Received in revised form 30 April 2009
Accepted 3 May 2009

*Keywords:*
fMRI
Functional connectivity
Voxel correlation
MRI preprocessing
*k*-Space preprocessing
Image processing

ABSTRACT

Image processing is common in functional magnetic resonance imaging (fMRI) and functional connectivity magnetic resonance imaging (fcMRI). Such processing may have deleterious effects on statistical maps computed from the processed images. In this manuscript, we describe a mathematical framework to evaluate the effects of image processing on observed voxel means, covariances and correlations resulting from linear processes on *k*-space and image-space data. We develop linear operators for common image processing operations, including: zero-filling, apodization, smoothing and partial Fourier reconstruction; and unmodeled physical processes, including: Fourier encoding anomalies caused by eddy currents, intra-acquisition decay and magnetic field inhomogeneities. With such operators, we theoretically compute the exact image-space means, covariances and correlations which result from their common implementation and verify their behavior in experimental phantom data. Thus, a very powerful framework is described to consider the effects of image processing on observed voxel means, covariances and correlations. With this framework, researchers can theoretically consider observed voxel correlations while understanding the extent of artifactual correlations resulting from image processing. Furthermore, this framework may be utilized in the future to theoretically optimize image acquisition parameters, and examine the order of image processing steps.



## 1. Introduction

Magnetic field gradients can be used in magnetic resonance imaging to encode the measured signal as a linear transformation of the object being imaged. An inverse transform is then applied to the acquired signal to reconstruct an image of the object. As the encoding and reconstruction are linear transformations, they can be considered through the constructs of linear algebra as multiplications of matrices upon vectors representing either the physical object or the acquired signal. Rowe et al. (2007) have recently published a description of this mathematical formalism, using Fourier encoding and reconstruction as a specific example. In the case of Fourier encoding, the acquired data is in the spatial frequency space, *k*-space, and it is reconstructed through the inverse Fourier transform to image-space. In addition to describing the mathematical formalism of image reconstruction, the work also illustrated that, because of the linear properties of the reconstruction, correlated observations in *k*-space lead to correlated volume elements, or voxels, in the reconstructed image.

Correlated voxels, which necessarily arise from correlated *k*-space measurements, are the basis of functional connectivity studies (Biswal et al., 1995). These connectivity studies determine voxels to be connected if their time series exhibit high correlations. Common techniques, including cross-correlation analysis, principle component analysis (PCA), and independent component analysis (ICA), have been used to determine regions with high correlations in their time series (Biswal et al., 1995; Friston et al., 1993; van de Ven et al., 2004). Regardless of the analysis method, voxel correlation, and thus *k*-space correlation, affect the measured voxel connectivity.

The low temporal frequency physiologic processes upon which functional connectivity studies rely are clearly not the only sources of voxel correlation. Global signal fluctuation may arise from physiologic processes (Glover et al., 2000; Pfeuffer et al., 2002; Birn et al., 2006; Shmueli et al., 2007). As described by Rowe et al. (2007), temporal autocorrelation in the acquired signal also may lead to image-space voxel correlation. Artifactual time series correlations have also been observed in inanimate phantom stud-

* Corresponding author at: Department of Biophysics, Medical College of Wisconsin, 8701 Watertown Plank Road, Milwaukee, WI 53226, USA.
Tel.: +1 414 456 4027; fax: +1 414 456 6512.
*E-mail address:* dbrowe@mcw.edu (D.B. Rowe).

0165-0270/$ – see front matter © 2009 Elsevier B.V. All rights reserved.
doi:10.1016/j.jneumeth.2009.05.007

ies (Kriegeskorte et al., 2008). Additionally, as this manuscript describes, operations on *k*-space data before reconstruction and image-space data after reconstruction can produce correlations in voxels. Sequences of spatially correlated images lead to temporally correlated time series. Clearly one must be mindful of the effects of such operations when drawing conclusions from functional connectivity (fcMRI) and functional (fMRI) data.

In this manuscript we consider several operations. These include: Fourier encoding anomalies, *k*-space observation censoring, *k*-space line shifting, symmetric *k*-space generation, and smoothing through *k*-space windowing, zero-filling, and image-space convolution. We first develop linear operators for the mentioned operations and show toy examples of each using an $8 \times 8$ data set. We then utilize the operators to theoretically examine image-space correlations associated with the operators under more relevant parametrizations, including $96 \times 96$ data acquisition arrays. Finally we illustrate the results of the operations in acquired $96 \times 96$ phantom data.

## 2. Theory

### 2.1. Operator development

In this section we extend the mathematical formalism of image reconstruction presented by Rowe et al. (2007) to a more general case. We describe Cartesian Fourier reconstruction for the sake of demonstration, although the mathematics hold true for any linear reconstruction operator. Other linear operators may include regridding operators for non-Cartesian *k*-space sampling methods. First we further extend the previously published statistical model to include the data as it is ideally collected. This includes modeling the points acquired during the phase encoding blips of echo planar imaging (EPI), and the reversal of lines acquired with negative frequency encoding gradients. We describe models of Fourier encoding anomalies, *k*-space line shifting, symmetric *k*-space generation, zero-filling, and multiplication of the *k*-space observations with a windowing function in light of the extended statistical model.

Rowe et al. (2007) have described complex-valued Fourier reconstruction through a real-valued isomorphism such that a vector of the reconstructed image, $y$, is the product of a Fourier reconstruction operator, $\Omega$, with a vector of the observed *k*-space observations, $s$:

$$y = \Omega s. \tag{1}$$

In the above equation, if the reconstructed image is $m$ rows by $n$ columns, $y$ is a vector with $mn$ real image values stacked above $mn$ imaginary image values, $\Omega$ is a reconstruction operator array with dimensions of $2mn \times 2mn$, and $s$ is a vector of $mn$ appropriately ordered real Cartesian *k*-space observations stacked above $mn$ imaginary Cartesian *k*-space observations. The Cartesian Fourier reconstruction operator may be written as

$$\Omega = \begin{pmatrix} \Re(\Omega_C) & -\Im(\Omega_C) \\ \Im(\Omega_C) & \Re(\Omega_C) \end{pmatrix}, \tag{2}$$

where $\Re(\cdot)$ and $\Im(\cdot)$ take the real and imaginary parts of the arguments respectively, and $\Omega_C$ is the Kronecker product of two matrices, $\Omega_x$ and $\Omega_y$, which Fourier transform the columns and rows of the acquired *k*-space, respectively:

$$\Omega_C = \Omega_x \otimes \Omega_y.$$

The Kronecker product, denoted by $\otimes$, multiplies each element of the first matrix by the entire second matrix. The $jk$th element of $\Omega_x$, where $j$ and $k$ are indices from 0 to $n-1$, may be written as

$$(\Omega_x)_{jk} = w^{((-n/2)+j)((-n/2)+k)},$$

where $w = (1/n)e^{i2\pi/n}$ for the inverse Fourier transform and $w = e^{-i2\pi/n}$ for the forward Fourier transform. A similar matrix of dimension m exists for $\Omega_y$.

Under the formalism of Eq. (1), if the *k*-space observations have a covariance matrix of $\mathrm{cov}(s) = \Gamma_0$, the resulting reconstructed image-space values have a covariance matrix of $\Omega\Gamma_0\Omega^T$, where $T$ denotes transposition. Here we develop operators, $O$, such that the acquired signal, $S$, may be processed as desired and transformed to image-space. It is helpful to note that $s$ represents the properly ordered *k*-space data while $S$ represents the real/imaginary *k*-space observation pairs acquired along the *k*-space trajectory, including points acquired during echo planar imaging phase encoding blips. With such operators developed, the original reconstruction relationship shown in Eq. (1) may be more appropriately modeled as

$$y = OS, \tag{3}$$

with a covariance matrix resulting from the *k*-space covariance matrix, $\Gamma$, calculated as

$$\mathrm{cov}(y) = O\Gamma O^T. \tag{4}$$

In light of the new parameterization, if the originally collected *k*-space data, $S$, has mean of $S_0$, the final reconstructed complex-valued image, $y$, has a mean of $OS_0$ and a covariance matrix as shown above.

The covariance structure of the square of the magnitude data may be derived from this complex data covariance matrix. The covariance matrix for the square of the magnitude data is considered as an analytical solution exists in the described linear framework. The magnitude operation, being non-linear in nature, does not extend well to the described framework. Nevertheless, it can be shown that the magnitude squared covariance asymptotically approaches the magnitude covariance. It will be seen that the magnitude squared correlation structure, which is asymptotically equal to the magnitude data correlation structure, is generally found to exhibit similar properties to the real and imaginary correlation structures. A brief derivation of the magnitude squared covariance matrix is included in Appendix A.

In light of this framework, the effects of several processing techniques will be considered. The mean, covariance, and correlations will be computed for each operation on the complex and magnitude squared data. A brief description of each operator follows, with expanded descriptions of their compositions included in Appendices.

#### 2.1.1. Anomalies in Fourier encoding

The *k*-space observation process is often assumed to be instantaneous at the echo time, $TE$ (Haacke et al., 1999). Under that assumption, and assuming an exponential intra-acquisiton decay map of $T_2^*(x,y)$ and magnetic field inhomogeneity map of $\Delta B(x,y)$, the acquired *k*-space signal is

$$s(k_x,k_y) = \int_{-\infty}^{\infty}\int_{-\infty}^{\infty} \rho(x,y)e^{-TE/T_2^*(x,y)}e^{i\gamma\Delta B(x,y)TE}e^{-i2\pi(k_x x+k_y y)}\mathrm{d}x\mathrm{d}y, \tag{5}$$

where $\gamma$ is the proton gyromagnetic ratio and $\rho$ is the proton spin density. The *k*-space points are defined by the temporal integral of the applied magnetic field gradients applied along the appropriate directions:

$$k_x = \frac{\gamma}{2\pi}\int_0^t G_x(t')\mathrm{d}t', \quad k_y = \frac{\gamma}{2\pi}\int_0^t G_y(t')\mathrm{d}t'.$$

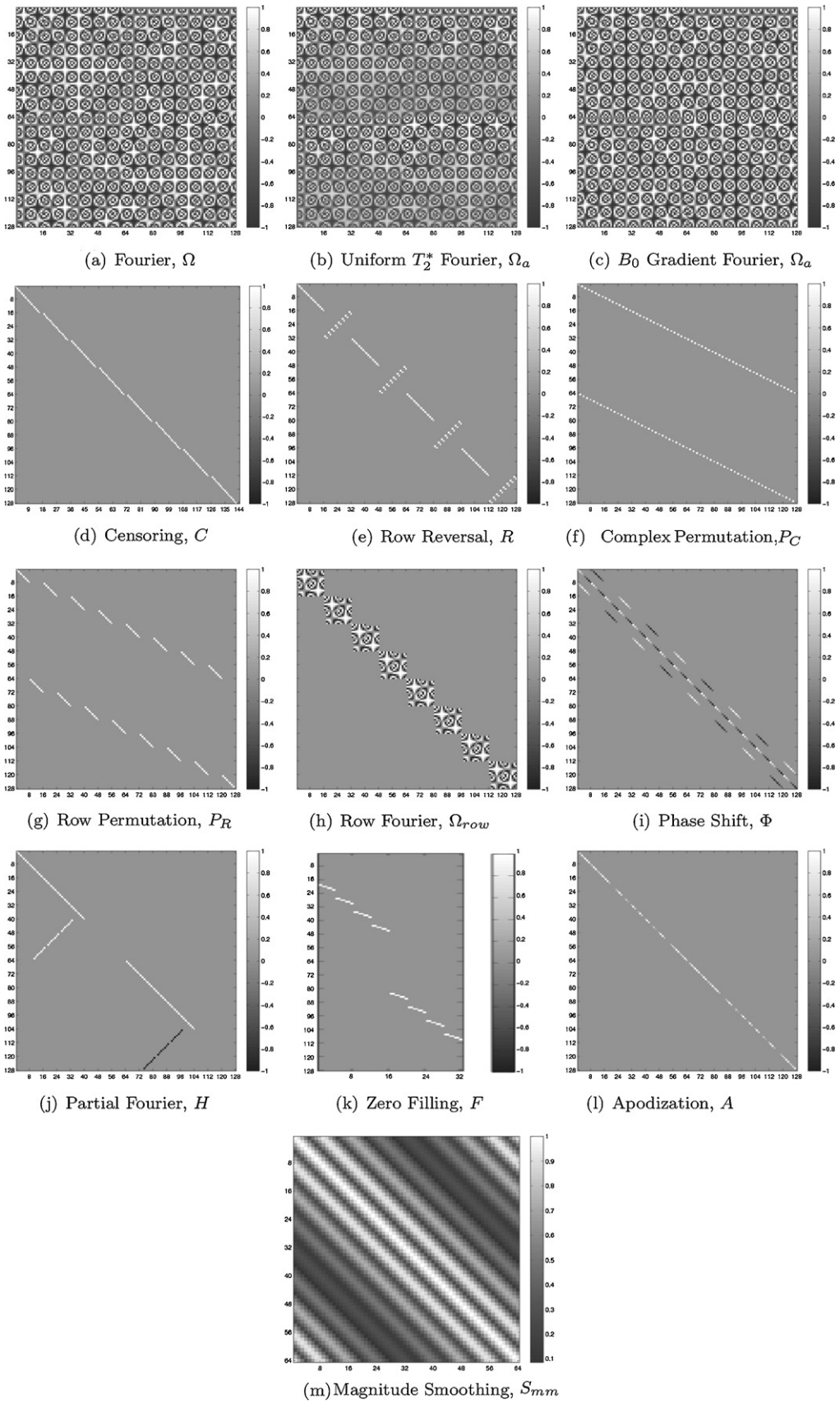


**Fig. 1.** Toy example operators. (a) Fourier, $\Omega$; (b) unifrom $T_2^*$ Fourier, $\Omega_a$; (c) $B_0$ gradient Fourier, $\Omega_a$; (d) censoring, $C$; (e) row reversal, $R$; (f) complex permutation, $P_C$; (g) row permutation, $P_R$; (h) row Fourier, $\Omega_{row}$; (i) phase shift, $\Phi$; (j) partial Fourier, $H$; (k) zero-filling, $F$; (l) apodization, $A$; (m) magnitude smoothing, $S_{mm}$.

Thus, the observed $k$-space data, encoded in time, is assumed to be the Fourier transform of the proton spin density weighted by the intra-acquisition decay and with a phase determined by the magnetic field inhomogeneity. The image-space representation may then be recovered with an inverse Fourier transform. An image of the ideal $128 \times 128$ Fourier, $\Omega$, operator, described above and in Rowe et al. (2007), for an $8 \times 8$ image array toy example is shown in Fig. 1(a). Each column of this operator corresponds to either the real or imaginary part of a voxel of the original $8 \times 8$ image array, and each row corresponds to either the real or imaginary part of a voxel of the processed image array. This operator is described as ideal as it does not account for $T_2^*$ or $\Delta B$ effects.

However, as the definition of $k$-space locations suggests, the $k$-space observation process occurs over a finite duration of time, with each $k$-space measurement being sampled at a unique time point. Thus, the $k$-space signal equation may be more appropriately considered as

$$s(k_x, k_y|t) = \int_{-\infty}^{\infty}\int_{-\infty}^{\infty} \rho(x,y) e^{-t/T_2^*(x,y)} e^{i\gamma\Delta B(x,y)t} e^{-i2\pi(k_x x + k_y y)} \mathrm{d}x\mathrm{d}y, \tag{6}$$

when the $k$-space point $(k_x, k_y)$ is sampled at time $t = t(k_x, k_y)$. With the $t(k_x, k_y)$ variable changing for each $k$-space measurement, image blurring from intra-acquisiton decay and image warping from magnetic field inhomogeneities may occur (Jesmanowicz et al., 1998; Jezzard and Balaban, 1995). Thus, the Fourier transform operator developed by Rowe et al. (2007) may be modified to account for non-instantaneous $k$-space observation in a modified Fourier operator, $\Omega_a$. Each row of the operator is modified with exponential terms for $T_2^*(x, y)$ and $\Delta B(x, y)$ as described in Appendix B.

The inclusions of these parameters finely alter the structure of $\Omega$ to arrive at $\Omega_a$. Two examples of $\Omega_a$ are shown in Fig 1(b) and (c). Fig. 1(b) illustrates a Fourier matrix that accounts for a spatially uniform $T_2^*$ decay. The element values tend toward zero in the later portion of $\Omega_a$ because of the exponential decay. Fig. 1(c) illustrates a Fourier matrix that accounts for a magnetic field gradient in the frequency encoding direction. This array is clearly different from the ideal Fourier array in Fig. 1(a) and the array including decay in Fig. 1(b). This Fourier array is essentially a skewed version of the ideal array. In both the cases of intra-acquisition decay and magnetic field inhomogeneity, an external measure of the perturber must be utilized. A $T_2^*(x, y)$ map may be acquired through the consideration of the magnitude of separate scans with varying echo times, and the $\Delta B(x, y)$ map may be acquired through the consideration of the phase of separate scans with varying echo times.

### 2.1.2. Obtaining s from S

In Eq. (1), $s$ is assumed to include only the properly ordered $k$-space observations located on the Cartesian $k$-space grid. However, as the $k$-space data is acquired in echo planar imaging (EPI), this is not true of the collected signal. Rather, the collected $k$-space data, $S$, is observed as real–imaginary pairs throughout the $k$-space traversal defined by the pulse sequence. Thus, in addition to including point-wise real–imaginary pairs instead of a column of real observations above a column of imaginary observations, the acquired data includes $e$ extra points acquired during the phase encoding blips and incorrectly ordered observations from the negative frequency encoding lines in echo planar imaging. If the acquired $k$-space point at row $r$ and column $c$ on the desired $k$-space grid is denoted as $s_{r,c,R/I}$, where the final $R/I$ index indicates that the observation is real or imaginary, and the extra $k$-space points acquired during the phase encoding blips are denoted as $E_{r,ep,R/I}$, with $ep$ indexing the extra point number, the actually acquired data is the long vector:

$$S = [s_{1,1,R}, s_{1,1,I}, \ldots, s_{1,n,I}, E_{1,1,R}, \ldots, E_{1,e,I}, s_{2,n,R}, s_{2,n,I}, s_{2,n-1,R}, \ldots, E_{m,e,I}]'.$$

However, the data required for the reconstruction in Eq. (1) is

$$s = [s_{1,1,R}, s_{1,2,R}, \ldots, s_{m,n,R}, s_{1,1,I}, \ldots, s_{m,n,I}]'.$$

Therefore, points in $S$ must be censored and its component lines reordered to produce the $s$ required in Eq. (1). This can be performed in the three steps of censoring extra points, reversing alternating lines, and segregating real and imaginary observations. Censoring may be performed with a censoring matrix, $C$, row reversal may be performed with a permutation matrix, $R$, and the separation of real and imaginary data may be performed with another permutation matrix, $P_C$. The construction of these operators is discussed in Appendix C, and the operators are shown in Fig. 1(d)–(f), respectively.

Thus, the process of converting the acquired data to the required data for Eq. (1) may be considered as

$$s = P_C R C S. \tag{7}$$

As the operators in Eq. (7) are censoring and permutation matrices, considering their effects on uncorrelated $k$-space observations is trivial. In the case of uncorrelated $k$-space observations, $\Gamma = I_{m(n+e)}$. The covariance between the processed $k$-space observations, $\Gamma_{P_C R C}$, is

$$\Gamma_{P_C R C} = P_C R C I_{m(n+e)} C^T R^T P_C^T$$
$$\Gamma_{P_C R C} = I_{mn}.$$

Thus, the processes of censoring, reversing, and permuting uncorrelated $k$-space observations does not yield correlated $k$-space values as it can be shown that $CC^{\mathrm{T}} = I$, $RR^T = I$ and $P_C P_C^T = I$. However, if identity $k$-space covariance matrix $\Gamma$ is not assumed, these processes will alter the covariance.

### 2.1.3. Line shifting

Unmodeled gradient timing errors and eddy current effects may cause alternating $k$-space lines to be shifted in EPI acquisitions (Haacke et al., 1999). This shifting results in the N/2 or Nyquist ghost artifact associated with EPI. An offset term is introduced in the signal equation:

$$s(k_x, k_y|t) = \int\int \rho(x,y) e^{-t/T_2^*(x,y) - i\gamma\Delta B(x,y)t + i(-1)^{\ell} 2\pi\Delta k_x x} e^{-i2\pi(k_x x + k_y y)} \mathrm{d}x\mathrm{d}y \tag{8}$$

where $\Delta k_x$ is the effective eddy current $k$-space shift and $\ell$ is the frequency encoding line number in Eq. (8). These shifts can be estimated and corrected to reduce such artifacts in the reconstructed images. Such shifts are often determined through the use of navigator echoes (Jesmanowicz et al., 1993) or reference scans Bernstein et al. (2004). Thus, opposite shifts are then applied to the acquired $k$-space lines to realign them. The application of these shifts involves the use of the Fourier shift theorem. Each line is Fourier transformed, multiplied by a complex-valued exponential, and then inverse Fourier transformed to the shifted state. Thus, the process of shifting the $k$-space lines can be considered in several steps: The vector $s$ is reordered to group real and imaginary observations from each line together; The lines are Fourier transformed; The transformed lines are multiplied by a complex-valued exponential; The phase altered lines are inverse Fourier transformed into shifted lines; The shifted lines are reordered to the original ordering of $s$. Thus, three operators need to be constructed: a permutation operator, $P_R$, to convert from $s$ with the reals for the image stacked above the imaginaries for the image to a vector of reals stacked above imaginaries for each row; a row Fourier transform operator, $\Omega_{row}$, to transform each of the rows; and a phase shift operator, $\Phi$, to alter the phase of the transformed rows. Additionally, inverses of

the permutation operator, trivially $P_R^{-1} = P_R^T$, and Fourier transform operator, $\Omega_{row}^{-1}$, are needed. The details of these three operators are given in Appendix D, and image representations of them are shown in Fig. 1(g)–(i).

With the permutation, Fourier transform and phase shift operators defined, shifting the acquired $k$-space lines alternating directions to yield a corrected set of $k$-space observations simply involves linear algebra:

$$s_{corrected} = P_R^{-1}\Omega_{row}^{-1}\Phi\Omega_{row}P_R s. \quad (9)$$

Thus, when performed on a time series of images, the reconstructed mean and covariance are altered by the processes in Eq. (9) to

$$E(y) = \Omega P_R^{-1}\Omega_{row}^{-1}\Phi\Omega_{row}P_R s_0 \quad (10)$$

and

$$\mathrm{cov}(y) = (\Omega P_R^{-1}\Omega_{row}^{-1}\Phi\Omega_{row}P_R)\Gamma(P_R^{-1}\Omega_{row}^{T}\Phi^T(\Omega_{row}^{-1})^T P_R\Omega^T), \quad (11)$$

where $s_0 = E(s)$ in Eq. (10) is the mean $k$-space observation vector and $\Gamma_0 = \mathrm{cov}(s)$ in Eq. (11) is the mean $k$-space covariance matrix. It should be once again noted that if $\Gamma = I$, then

$$(\Omega P_R^{-1}\Omega_{row}^{-1}\Phi\Omega_{row}P_R)(P_R^T\Omega_{row}^T\Phi^T(\Omega_{row}^{-1})^T(P_R^{-1})^T\Omega^T) = I \quad (12)$$

because it can be shown that each of the operators in Eq. (12) multiplied by their transposes yield identity matrices. If $\Gamma \neq I$, the mean, covariance, and correlation will be altered by the operations, leading to the correlation of a voxel with its ghost location.

#### 2.1.4. Symmetric k-space generation

Symmetric $k$-space generation relies upon the symmetry of $k$-space about the origin under complex conjugation when a real-valued object is imaged. This symmetric generation has been used in partial Fourier acquisitions (Jesmanowicz et al., 1998). In the simplest case the first $m/2+1$ lines of $k$-space are acquired and the final $m/2-1$ lines are generated through the symmetry relationship. The partial Fourier interpolation matrix, $H$, is described in Appendix E. A graphical representation of $H$ is shown in Fig. 1(j) for the case of an $8\times8$ symmetric $k$-space generation from a $5\times8$ $k$-space acquistion.

With this partial Fourier reconstruction matrix, the omitted data is generated using the $k$-space symmetry relationship with the matrix multiplication $s_S = Hs$. In the event of a full $k$-space acquisition, no symmetric data need be generated and $H = I$. Effects of partial Fourier processing on a data set may be considered with the modified reconstructed mean and covariance being

$$E(y) = \Omega H s_0$$

and

$$\mathrm{cov}(y) = \Omega H\Gamma_0 H^T\Omega^T. \quad (13)$$

Note that $HH^T \neq I$ when a partial $k$-space acquisition is made. It is seen that partial $k$-space reconstruction necessarily requires $k$-space observations to be correlated. Therefore, as the process of reconstruction is linear, image-space observations must exhibit a correlation. Thus, the operator modifies the covariance and correlation. Of course, the reconstruction of an image with fewer points in partial Fourier reconstruction additionally yields increased variance.

#### 2.1.5. Smoothing with k-space windowing and image-space convolution

Smoothing of the complex-valued data may be performed during apodization, zero-filling, or explicit image smoothing operations. The Fourier convolution theorem allows complex-valued image-space convolution to be considered with $k$-space windowing. Thus, zero-filling, $k$-space apodization, and image-space complex data smoothing may be considered with operators of the same form. Because of the image-space convolution associated with these processes, it is obvious that they have a non-negligible effect on image-space voxel correlations. In Appendix F, we describe a zero-filling operator, $F$, and an apodization operator, $A$. The apodization operator may include any windowing function, including the usual Fermi, Tukey, Hanning or Gaussian apodization windows. In Appendix F, we also describe an operator, $S_m$, which may be implemented on magnitude or magnitude squared data to yield image-space smoothing. The zero-filling operator is shown in Fig. 1(k), the apodization operator in Fig. 1(l), and the image-space magnitude smoothing operator in Fig. 1(m).

As it is well known, convolution alters the image mean, covariance, and correlation. Thus, even if $\Gamma = I$, the application of these operators alters the data as it will be shown.

## 3. Operator implementation

With the above linear operators defined, it is possible to mathematically determine the image-space correlations resulting from applying the operators to $k$-space data with a covariance matrix, $\mathrm{cov}(S) = \Gamma$. The image-space covariance, $\mathrm{cov}(y)$, after applying an operator, $O$, to $k$-space data with a covariance matrix of $\Gamma$ is defined in Eq. (4).

Without loss of generality, we describe here the case of applying the operators to uncorrelated $k$-space data. Thus, $\Gamma$ is assumed to be the identity matrix. Therefore, Eq. (4) simplifies to $\mathrm{cov}(y) = OO^T$. It is clear from this that if $OO^T = \delta^2 I$, where $\delta^2 = 1/(m^2n^2)$ is a scalar introduced by the inverse Fourier transform, then the resulting image-space observations have scaled identity covariance matrices. With the covariance matrix known, the correlation matrix may be exactly calculated as

$$\mathrm{cor}(y) = D^{-1/2}\mathrm{cov}(y)D^{-1/2}, \quad (14)$$

where $D = \mathrm{diag}(\mathrm{cov}(y))$.

As it was mentioned in the description of the operators, the censoring of the $k$-space observations, row reversal, reordering, and line shifting operators yield no image-space correlations in uncorrelated $k$-space data as in each case the operator multiplied by its transpose results in an identity matrix. If the $k$-space covariance matrix is not the identity, the operators will modify the covariance and correlation. More interesting results follow from the application of the operators including anomalies in the Fourier encoding process, partial Fourier reconstruction and $k$-space windowing or image-space convolution. In the following sections we consider these operators individually and serially in the case of a $96\times96$ data acquisition.

In the following calculations, physical parameters similar to those in typical fMRI studies were considered. The maps of the physical parameters and apodizers considered are shown in Fig. 2. The proton spin density, $\rho$ shown in Fig. 2(a), was assumed to be zero outside of the phantom, and unity within the phantom. The intra-acquisition decay, $T_2^*$ shown in Fig. 2(b), was considered as a modified Shepp–Logan phantom which was scaled to physically relevant values from 10 to 100 ms. The B field inhomogeneity was considered as a horizontal gradient from 0 to $2.5\times10^{-6}$ T, as shown in Fig. 2(c). This B field inhomogeneity is significant, but on the order of the inhomogeneity observed in the inferior frontal lobe. The timing of the $k$-space observations is shown in Fig. 2(d), and is representative of a standard EPI pulse sequence with an acquisition matrix of $96\times96$, bandwidth of 250 kHz, effective echo spacing of 0.96 ms, and echo time of 50 ms. The considered $k$-space apodization filter, shown in Fig. 2(e), is a Gaussian window with an image-space representation shown in Fig. 2(f). The image-space representation has a full width at half maximum of three pixels. Partial Fourier reconstruction was considered with 16 overscan lines.

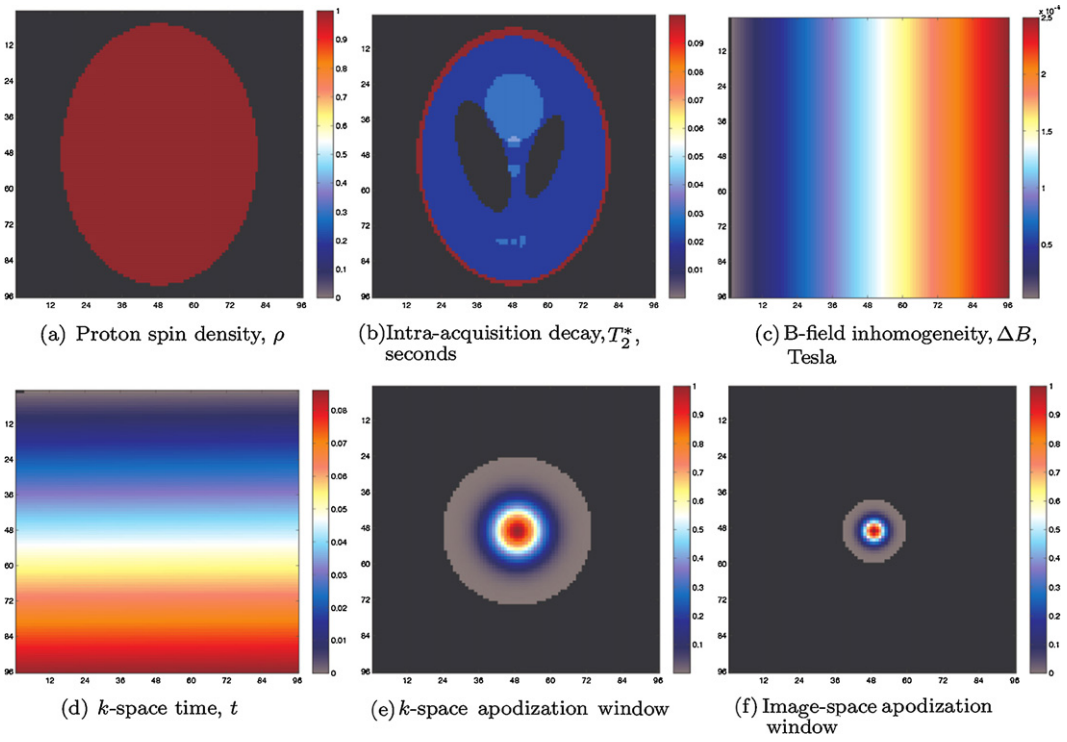


**Fig. 2.** Parameters considered in theoretical calculations. (a) Proton spin density, $\rho$; (b) intra-acquisition decay $T_2^*$, seconds; (c) B-field inhomogeneity, $\Delta B$, Tesla; (d) $k$-space time, $t$; (e) $k$-space time apodization window; (f) image-space apodization window.

When the processes were not considered in the following calculations the parameters for the unconsidered processes are equivalent to: $T_2^*$ as a uniform, infinite map; $\Delta B$ as a map of zeroes; and the apodization window as a map of ones.

Calculations were made to examine the intra-acquisition decay, B field inhomogeneity, partial Fourier interpolation, and $k$-space apodization operators individually. Additionally, the combination of intra-acquisition decay, partial Fourier interpolation and $k$-space apodization performed serially was evaluated. Results illustrating the processed image means are shown in Fig. 3, and the correlations for the center pixel in the processed images with all other pixels are shown in Fig. 4. The first and second columns of Fig. 3 illustrates the mean magnitude and phase images, while the third and fourth columns respectively illustrate the mean real and imaginary images. Each row of Fig. 3 illustrates the results on the mean image in light of a different processing pipeline. Fig. 4 illustrates the correlations for the center pixel for the same processing cases. Additionally, correlation coefficients for the four neighbors of the center pixel are shown in Table 1 for several processing pipelines.

### 3.1. Fourier anomalies

As it has previously been described, intra-acquisition decay yields an increase in the point spread function in the phase encoding direction (Jesmanowicz et al., 1998). The increase in the point spread function occurs preferentially in the phase encoding direction because of the decreased effective bandwidth in this direction in EPI. This can be seen through the apparent blurring of the edges of the phantom in the magnitude and real images in Fig. 3(a) and (c). Nevertheless, slight correlation is noted between voxels in the frequency encoding direction as well in Table 1 due to the non-instantaneous acquisition of each $k$-space line. These correlations are dramatically less in the frequency encoding direction than in the phase encoding direction because of the remarkably higher bandwidth in the frequency encoding direction. Additionally, intra-acquisition decay leads to the appearance of edges in the mean phase and imaginary image in Fig. 3(b) and (d). The increased point spread function in the phase encoding direction is clear in the correlation maps in Fig. 4(a)–(d). The magnitude squared point spread function is less than the real and imaginary point spread functions. Moderate correlation between the real and imaginary data was observed along the phase encoding direction. The observation of the reduced magnitude squared point spread function holds true for each of the considered processing pipelines.

Also as previously described, static B field inhomogeneities lead to image warping and phase generation (Jezzard and Balaban, 1995) Thus, warping and a bulk shift in the phase encoding direction is apparent in the mean images that include B field inhomogeneities in the Fourier operators in Fig. 3(e)–(h). More minor sub-voxel warping also occurs in the frequency encoding direction because of the higher sampling bandwidth in that direction. The phantom appears warped but uniform in Fig. 3(e) as the magnitude data does not contain phase information, while the horizontally varying phase information is apparent in the phase, real and imaginary data in Fig. 3(f)–(h). Very small correlations are seen from the B field inhomogeneity in Fig. 4(e)–(h). In fact, as seen in Table 1, higher correlation coefficients are observed in the frequency encoding direction than in the phase encoding direction. Such an observation may corroborate the observations of Kriegeskorte et al. (2008) where correlations in the frequency encoding direction appear to dominate. In this framework with uncorrelated data, B field inhomogeneities do not significantly alter observed variances.

### 3.2. Partial Fourier reconstruction

In the ideal calculated case, partial Fourier reconstruction does not visually alter the mean reconstructed images in Fig. 3(i)–(l). As expected with partial Fourier reconstruction, no obvious information is introduced into the phase or imaginary data. However, as described above, partial Fourier interpolation does slightly alter the mean image and correlation structure, even in this ideal case. Negligible correlation results between the real and imaginary data

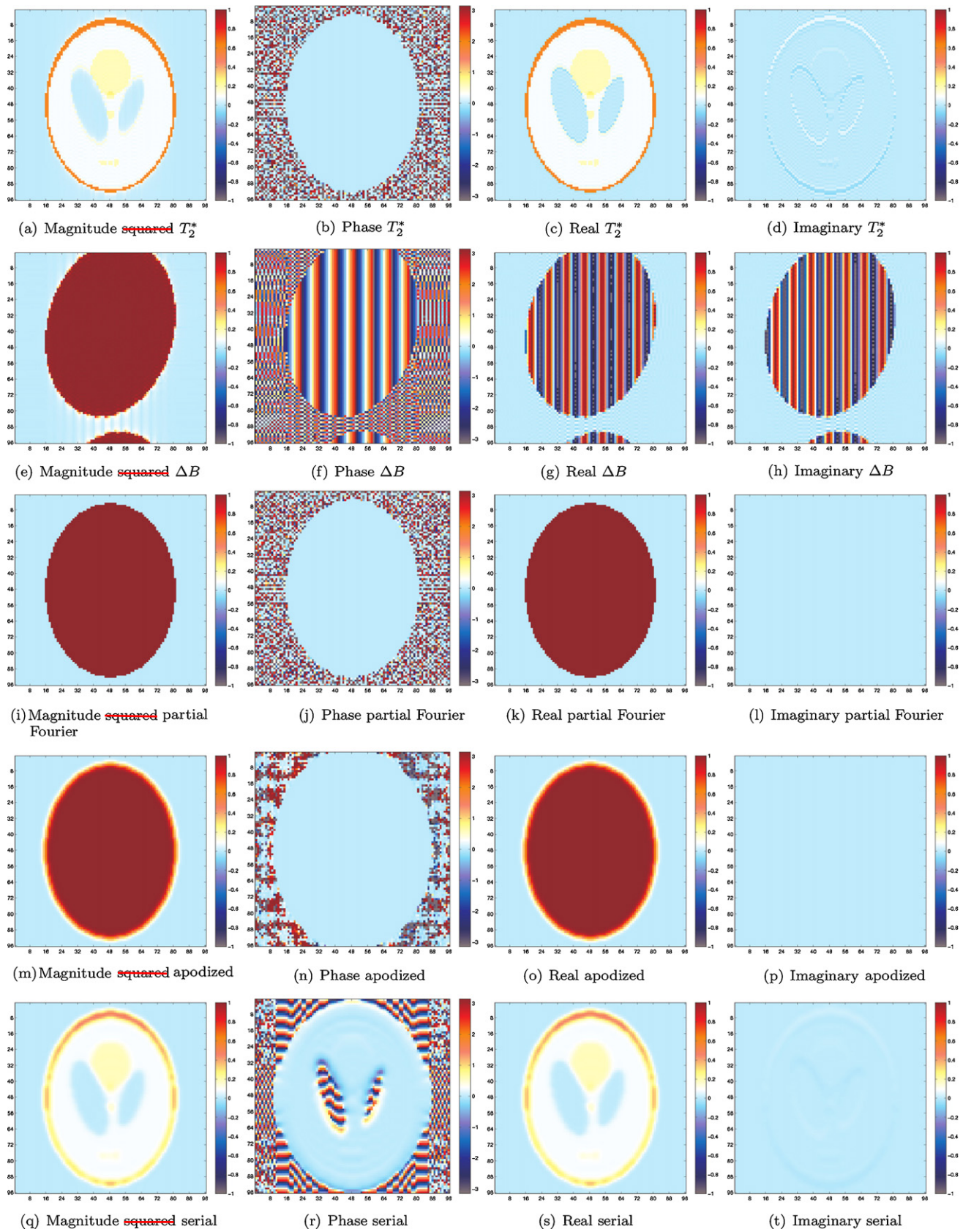


**Fig. 3.** Reconstructed mean magnitude squared, phase, real and imaginary signal with various processes included. In each case, only the listed operator was included. In the serial case, $T_2^*$ decay, partial Fourier reconstruction, and $k$-space apodization were considered. (a) Magnitude squared $T_2^*$; (b) phase $T_2^*$; (c) real $T_2^*$; (d) imaginary $T_2^*$; (e) magnitude squared $\Delta B$; (f) phase $\Delta B$; (g) real $\Delta B$; (h) imaginary $\Delta B$; (i) magnitude squared partial Fourier; (j) phase partial Fourier; (k) real partial Fourier; (l) imaginary partial Fourier; (m) magnitude squared apodized; (n) phase apodized; (o) real apodized; (p) imaginary apodized; (q) magnitude squared serial; (r) phase serial; (s) real serial; (t) imaginary serial.

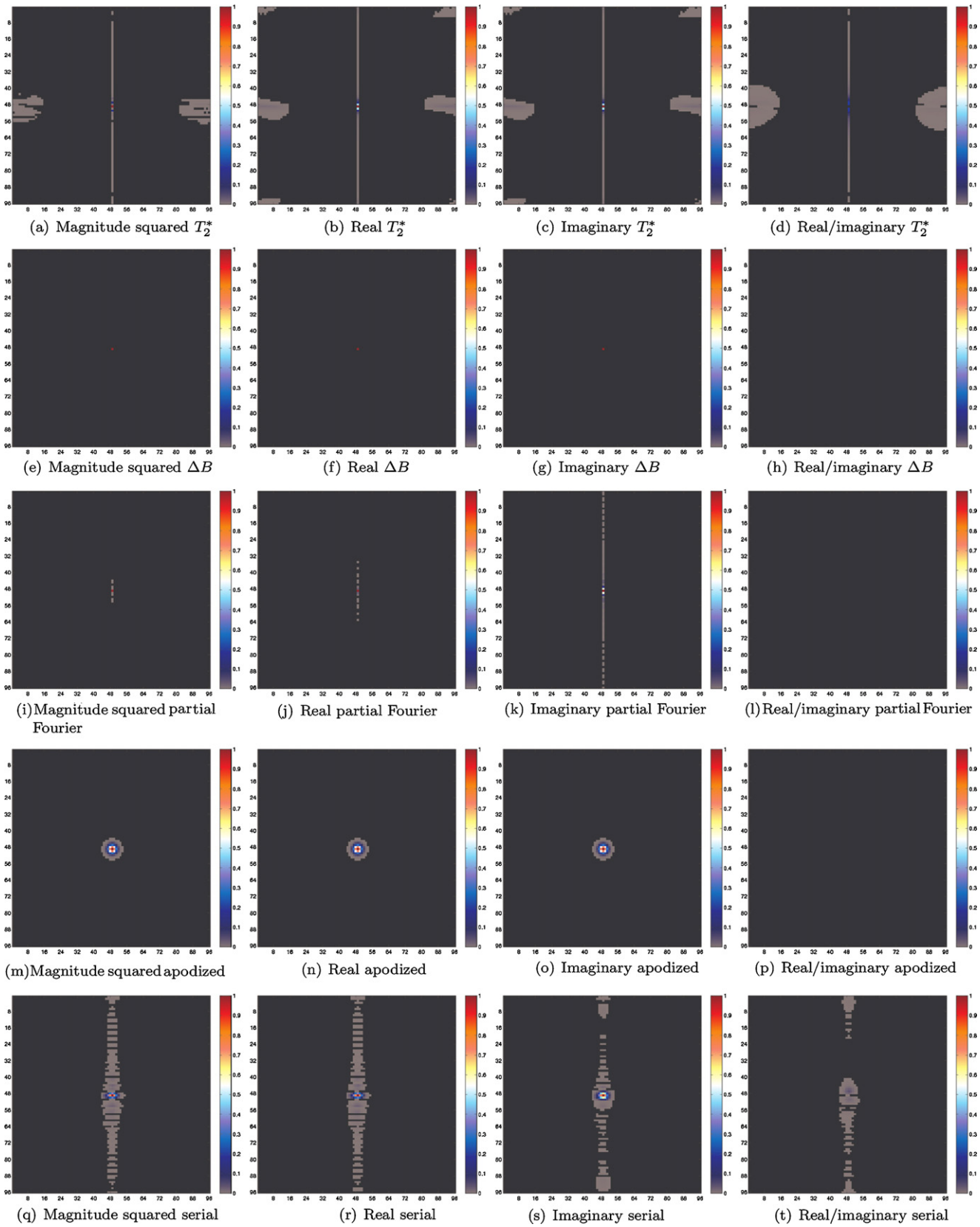


**Fig. 4.** Image-space correlations for the center pixel in magnitude squared, real, imaginary, and real/imaginary data with various processes included. In each case, only the listed operator was included. In the serial case, $T_2^*$ decay, partial Fourier reconstruction, and $k$-space apodization were considered. (a) Magnitude squared $T_2^*$; (b) real $T_2^*$; (c) imaginary $T_2^*$; (d) real/imaginary $T_2^*$; (e) magnitude squared $\Delta B$; (f) real $\Delta B$; (g) imaginary $\Delta B$; (h) real/imaginary $\Delta B$; (i) magnitude squared partial Fourier; (j) real partial Fourier; (k) imaginary partial Fourier; (l) real/imaginary partial Fourier; (m) magnitude squared apodized; (n) real apodized; (o) imaginary apodized; (p) real/imaginary apodized; (q) magnitude squared serial; (r) real serial; (s) imaginary serial; (t) real/imaginary serial.

**Table 1**
Calculated correlation coefficients for the center voxel's nearest neighbors under several operations.

| Operation | Left neighbor real | Left neighbor imaginary | Left neighbor real/imaginary | Left neighbor magnitude$^2$ | Right neighbor real | Right neighbor imaginary | Right neighbor real/imaginary | Right neighbor magnitude$^2$ |
|---|---|---|---|---|---|---|---|---|
| None | 1.3e−16 | 1.3e−16 | 4.25e−17 | 3.3e−17 | 1.3e−16 | 1.3e−16 | 4.25e−17 | 3.3e−17 |
| Uniform $T_2^*$ | 5.6e−8 | 5.6e−8 | 3.7e−5 | 1.2e−8 | 5.6e−8 | 5.6e−8 | 3.7e−5 | 1.2e−8 |
| Varying $T_2^*$ | 4.9e−8 | 4.9e−8 | 3.4e−5 | 1.6e−8 | 4.9e−8 | 4.9e−8 | 3.4e−5 | 1.2e−8 |
| B-gradient | 5.5e−7 | 5.5e−7 | 5.8e−10 | 7.5e−8 | 5.5e−7 | 5.5e−7 | 6.0e−10 | 7.7e−10 |
| Partial Fourier | 3.8e−5 | 8.9e−5 | 8.0e−17 | 7.0e−6 | 3.8e−5 | 8.9e−5 | 8.0e−17 | 7.0e−6 |
| Partial Fourier and uniform $T_2^*$ | 5.6e−5 | 4.0e−3 | 1.3e−6 | 1.3e−6 | 5.6e−5 | 4.0e−3 | 1.3e−6 | 1.3e−6 |
| Partial Fourier and varying $T_2^*$ | 7.7e−5 | 8.6e−4 | 9.3e−7 | 2.3e−6 | 7.7e−5 | 8.7e−4 | 1.3e−6 | 2.3e−6 |
| Gaussian smoothing | 7.3e−1 | 7.3e−1 | 1.3e−16 | 7.3e−1 | 7.3e−1 | 7.3e−1 | 1.3e−16 | 7.3e−1 |
| Varying $T_2^*$ partial Fourier and smoothing | 7.5e−1 | 7.5e−1 | 2.2e−4 | 7.5e−1 | 7.4e−1 | 7.4e−1 | 1.0e−4 | 7.4e−1 |
| Varying $T_2^*$ B-gradient and smoothing | 8.2e−1 | 8.2e−1 | 2.9e−6 | 7.0e−1 | 7.5e−1 | 7.5e−1 | 2.7e−6 | 5.4e−1 |

| Operation | Top neighbor real | Top neighbor imaginary | Top neighbor real/imaginary | Top neighbor magnitude$^2$ | Bottom neighbor real | Bottom neighbor imaginary | Bottom neighbor real/imaginary | Bottom neighbor magnitude$^2$ |
|---|---|---|---|---|---|---|---|---|
| None | 5.4e−15 | 5.4e−15 | 9.2e−15 | 1.4e−15 | 5.4e−15 | 5.4e−15 | 9.2e−15 | 1.4e−15 |
| Uniform $T_2^*$ | 4.9e−1 | 4.9e−1 | 2.0e−1 | 3.4e−3 | 4.9e−1 | 4.9e−1 | 2.0e−1 | 2.4e−3 |
| Varying $T_2^*$ | 4.9e−1 | 4.9e−1 | 1.9e−1 | 5.2e−3 | 4.9e−1 | 4.9e−1 | 1.9e−1 | 3.6e−3 |
| B-gradient | 2.7e−16 | 6.3e−17 | 8.1e−15 | 3.6e−17 | 1.5e−15 | 6.2e−20 | 1.1e−14 | 3.9e−16 |
| Partial Fourier | 2.6e−2 | 5.7e−1 | 1.0e−5 | 2.9e−3 | 2.6e−2 | 5.7e−1 | 1.0e−5 | 2.9e−3 |
| Partial Fourier and uniform $T_2^*$ | 5.3e−1 | 2.0e−1 | 1.1e−3 | 1.2e−1 | 5.3e−1 | 2.0e−1 | 1.1e−3 | 1.2e−1 |
| Partial Fourier and varying $T_2^*$ | 5.3e−1 | 1.1e−1 | 1.3e−3 | 1.0e−1 | 5.3e−1 | 1.1e−1 | 4.4e−4 | 1.2e−1 |
| Gaussian smoothing | 7.3e−1 | 7.3e−1 | 2.8e−16 | 7.3e−1 | 7.3e−1 | 7.3e−1 | 2.8e−16 | 7.3e−1 |
| Varying $T_2^*$ partial Fourier and smoothing | 3.7e−1 | 6.1e−1 | 2.2e−2 | 3.7e−1 | 3.3e−1 | 6.1e−1 | 1.1e−2 | 3.3e−1 |
| Varying $T_2^*$ B-gradient and smoothing | 5.9e−1 | 5.9e−1 | 1.4e−1 | 5.8e−1 | 5.9e−1 | 5.9e−9 | 1.4e−1 | 5.9e−1 |

**Table 2**
Correlation coefficients for the center voxel's nearest neighbors under several operations in experimental phantom data.

| Operation | Left neighbor real | Left neighbor imaginary | Left neighbor real/imaginary | Left neighbor magnitude$^2$ | Right neighbor real | Right neighbor imaginary | Right neighbor real/imaginary | Right neighbor magnitude$^2$ |
|---|---|---|---|---|---|---|---|---|
| No RF, no processing | 1.6e−4 | 5.6e−4 | 1.4e−5 | 3.1e−4 | 1.8e−4 | 1.3e−4 | 8.0e−4 | 4.0e−4 |
| Excitation | 2.0e−5 | 1.2e−3 | 2.5e−3 | 2.9e−7 | 3.7e−4 | 1.6e−3 | 6.7e−10 | 8.3e−4 |
| No RF, partial Fourier | 1.2e−3 | 2.2e−3 | 2.2e−3 | 2.8e−4 | 2.3e−4 | 5.0e−4 | 1.9e−4 | 1.3e−4 |
| Excitation, partial Fourier | 2.5e−4 | 1.3e−4 | 4.4e−3 | 2.8e−4 | 1.1e−3 | 3.6e−4 | 8.0e−6 | 9.7e−4 |
| No RF, smoothing, | 9.3e−1 | 9.3e−1 | 1.4e−5 | 8.7e−1 | 9.3e−1 | 9.4e−1 | 4.9e−4 | 8.7e−1 |
| Excitation, smoothing | 9.8e−1 | 9.5e−1 | 1.2e−1 | 9.8e−1 | 9.8e−1 | 9.6e−1 | 2.3e−1 | 9.8e−1 |
| Operation | Top neighbor real | Top neighbor imaginary | Top neighbor real/imaginary | Top neighbor magnitude$^2$ | Bottom neighbor real | Bottom neighbor imaginary | Bottom neighbor real/imaginary | Bottom neighbor magnitude$^2$ |
| No RF, no processing | 6.6e−3 | 2.1e−3 | 1.9e−5 | 1.8e−3 | 1.3e−4 | 1.1e−3 | 1.9e−3 | 1.1e−5 |
| Excitation | 1.4e−4 | 1.9e−5 | 3.2e−4 | 3.2e−4 | 1.9e−3 | 2.2e−3 | 4.1e−5 | 1.4e−3 |
| No RF, partial Fourier | 1.2e−4 | 1.7e−3 | 6.3e−4 | 3.2e−3 | 1.0e−3 | 1.7e−3 | 5.1e−5 | 1.1e−7 |
| Excitation, partial Fourier | 8.2e−4 | 7.4e−5 | 7.0e−4 | 7.7e−4 | 1.2e−3 | 8.7e−4 | 1.6e−4 | 1.3e−3 |
| No RF, smoothing | 9.4e−1 | 9.3e−1 | 7.9e−4 | 8.8e−1 | 9.4e−1 | 9.4e−1 | 4.9e−6 | 8.8e−1 |
| Excitation, smoothing | 9.7e−1 | 9.6e−1 | 1.6e−1 | 9.8e−1 | 9.7e−1 | 9.6e−1 | 1.6e−1 | 9.7e−1 |

as seen in Fig. 4(l). Fig. 4(i)–(k) illustrate slight correlations in the phase encode direction. Note that these correlations are less than those associated with intra-acquisition decay. In fact, as previously described by Jesmanowicz et al. (1998), when both partial Fourier reconstruction and intra-acquisition decay are considered, reduced correlation along the phase encoding direction is observed when compared to full Fourier reconstruction in the presence of intra-acquisition decay. Although Table 1 shows slight increases in correlation coefficients in neighboring voxels in the phase encoding direction with partial Fourier reconstruction, the effective point spread function in the phase encoding direction is reduced by partial Fourier reconstruction. It should be further noted that non-zero phase, caused by magnetic field inhomogeneities, exists in experimental data and leads to further alterations of the reconstructed mean images. Partial Fourier reconstruction was found to increase variance in the real and magnitude data while decreasing variance in the imaginary data, as expected.

### 3.3. *k*-Space windowing and image-space convolution

Apodization with a Gaussian window clearly alters the reconstructed image means. The magnitude mean image in Fig. 3(m) illustrates that the edge of the phantom is blurred and dilated as a result of convolution of the image-space apodization kernel. The real mean image shows the same result in Fig. 3(o). As there is ideally no data in the imaginary data, apodization does not introduce significant information into the phase and imaginary mean images in Fig. 3(n) and (p), although the noise appears to be smoothed. Correlations resulting from apodization, shown in Fig. 4(m)–(p), are as expected through the Fourier convolution theorem. Specifically, the image-space correlations resulting from *k*-space apodization are related to the image-space convolution with the Fourier transform of the *k*-space apodization window. As convolution with a real-valued kernel does not induce correlations between the real and imaginary data, no correlations are seen in Fig. 4(p). Apodization was found to decrease variance as expected with spatial smoothing.

### 3.4. Serial processes

The results of serially considering intra-acquisition decay, partial Fourier reconstruction, and *k*-space apodization on the mean images are shown in Fig. 3(q)–(t). The effects of intra-acquisition decay and apodization appear to dominate the reconstructed mean images. However, the computed image-space correlations, shown in Fig. 4(q)–(t), are not simply the superposition of the correlations associated with each process. In this result, some of the utility of the theoretical framework is illustrated as the result of a series of complicated processing steps may be easily computed. The effects of smoothing from apodization were found to dominate the processed data variance as it was reduced to the level observed with apodization alone.

## 4. Experimental illustration

To illustrate the performance of the operators, their application to phantom data was considered. Two experimental data sets were considered. The data sets were acquired on a 3.0 T General Electric Signa LX magnetic resonance imager, with a spherical doped agar phantom with $T_2^* = 40.0$ ms as the subject. Each data set consisted of 1024 images of a single 2.5 mm thick, 24.0 cm field of view slice, with a $96 \times 96$ acquisition matrix, minimum full *k*-space echo time of 50.0 ms, effective echo spacing of 0.96 ms, 2000.0 ms repetition time, and 250 kHz acquisition bandwidth. The proton spins were excited with an 80° radio frequency pulse in one data set, and with a 0° radio frequency pulse in the other data set. The data set with no excitation pulse was acquired to match the condition of pure

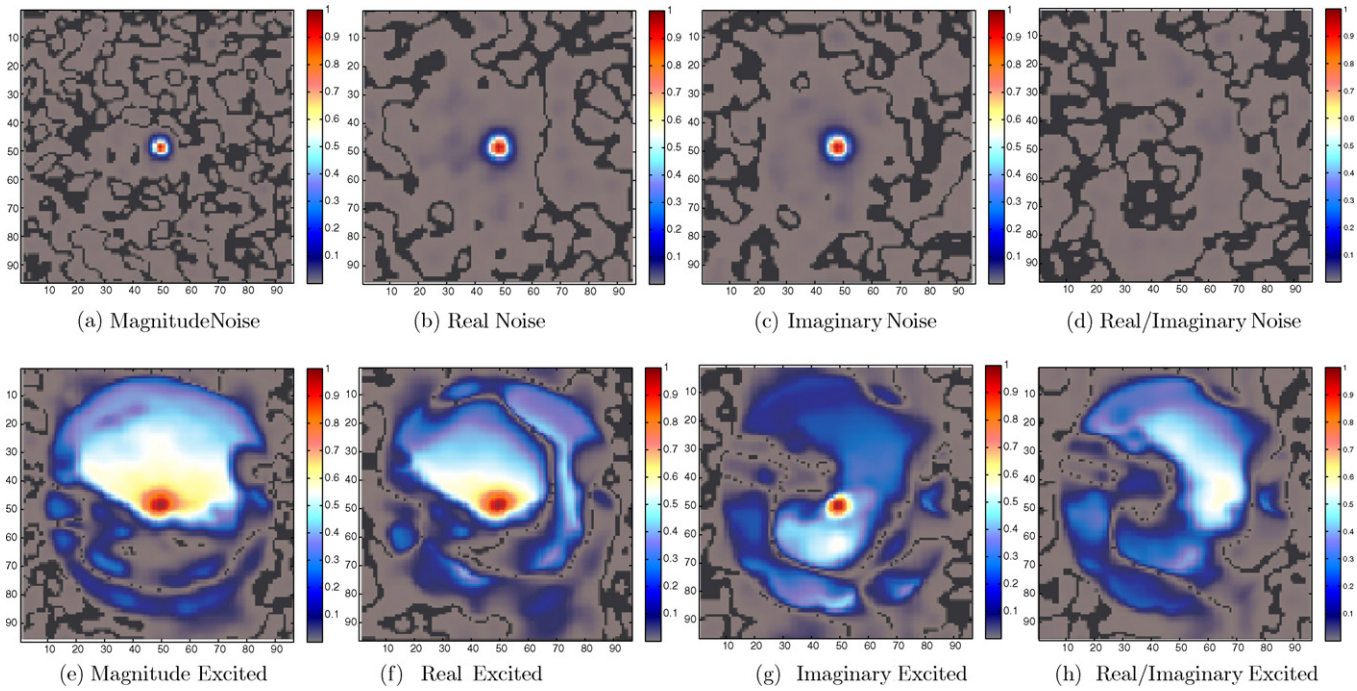


**Fig. 5.** Image-space correlations for the center voxel in the acquired phantom data with no excitation pulse (noise) and with an excitation pulse (excited) in the magnitude squared, real, imaginary, and real/imaginary data after smoothing. (a) Magnitude noise; (b) real noise; (c) imaginary noise; (d) real/imaginary noise; (e) magnitude excited; (f) real excited; (g) imaginary excited; (h) real/imaginary excited.

noise considered in some of the above theoretical computations, while the data set with an excitation pulse more closely matches standard acquisitions.

Data were collected with a custom echo planar imaging pulse sequence, and reconstructed with locally developed software. With control of the entire acquisition and reconstruction pipeline, the confounds of unmodeled data processing are reduced. Nevertheless, some temporal filtering of the *k*-space acquisitions is performed to sub-sample the acquired 1 GHz samples to the collected 250 kHz samples. This processing may result in an auto-correlation of *k*-space observations, although such a correlation structure was not observed and is likely obscured by the noise in the experimental data.

Three navigator echoes of the center line of *k*-space were acquired to estimate error in the center frequency, and group delay offsets between odd and even *k*-space lines (Nencka et al., 2008). In the data acquired with an excitation pulse a group delay of 5.6 μs (1.4 *k*-space points) between odd and even lines was observed. Without correction of the group delay, severe Nyquist ghosting existed in the reconstructed data. This resulted in correlations between image voxels and ghost voxels. Correction of the group delay error greatly reduced the Nyquist ghost and resulting image-space correlations. The same group delay error was assumed on the data set acquired without an excitation pulse. No significant image-space correlations were apparent before or after application of the group delay error correction, in agreement with the theoretical result that the even and odd line shifts do not induce correlation in pure noise data. The data acquired with no radio frequency excitation was found to exhibit uncorrelated normally distributed noise in space and time with a mean of zero. Global, temporal phase structure was corrected in the data set acquired with radio frequency excitation to account for field shifts associated with gradient heating and radio frequency phase variation (Hahn et al., 2008). The data acquired with radio frequency excitation exhibited uncorrelated noise after phase correction. Thus, in both the no radio frequency excitation and the dynamic phase corrected data sets, there are no apparent structured correlations above the background correlations in the unprocessed data. Correlation coefficients in the experimental data for the four-neighbors of the center voxel under multiple processing conditions are shown in Table 2.

Smoothing of the noise data yields expected results, in agreement with those which are theoretically computed. The resulting images are shown in Fig. 5. The similarity between the magnitude squared, real, imaginary, and real/imaginary correlations in the smoothed noise data in Fig. 5(a–d) and the theoretical cases in Fig. 4(m–p) supports the validity of the theoretical method. Some residual phase correlation manifests itself in the correlation maps for the radio frequency excited data in Fig. 5(e–h). Nevertheless, these results are similar to the theoretically expected case.

## 5. Discussion

This work extends a line of research which has been briefly mentioned in a paper (Rowe et al., 2007), and further developed in conference proceedings (Nencka and Rowe, 2007, 2008). In that work, the underlying theory for computing image-space correlations based upon *k*-space processes was developed. We have extended that work by developing multiple operators for common reconstruction processes which are defined in the first part of this manuscript. We have studied the results of those operators by theoretically computing image-space correlations associated with relevant implementations. We have examined the validity of the operators and the theoretical image-space correlations by verifying the results in acquired phantom data.

The results presented in this manuscript for individual operations may appear obvious, as relatively simple operations were considered. However, the utility of the method is demonstrated when multiple operations are considered at once. With this theoretical framework, the exact image-space point spread function may be computed following a string of processing operations on ideally uncorrelated data. This is useful as often a string of operations are performed on a data set. If all the common processes

described here are implemented on a data set, the reconstructed image would be represented as

$$y = S_m \Omega_a A F H P_R^{-1} \Omega_{row}^{-1} \Phi \Omega_{row} P_R P_C R C S. \quad (15)$$

The complicated process including all the described processing steps in Eq. (15) lends itself well to this analytic mathematical model that is based upon simple linear algebra.

Furthermore, the alterations to an arbitrary covariance structure, $\Gamma$, may be examined. By computing the correlation structure following processing procedures on uncorrelated data, a reasonable null hypothesis threshold for experimental correlations may be considered. Thus, the theoretical method described in this manuscript and previous abstracts may be used to consider how much spatial processing is too much when considering functional connectivity or fMRI data.

This method may be further expanded with operators for additional processing operations. Operators for parallel acquisition image reconstruction, transmit/receive field inhomogeneities, non-cartesian gridding, masking, and image shifting could easily be developed for the described framework. Additionally, continuing work seeks to further extend this model to include more relevant temporal processing. A time series of images could be considered by stacking $k$-space observation vectors to create a time series observation vector, and performing Kronecker products between the operators and identity matrices with dimensions equal to the number of time series observations. Under such a parameterization, the effects of temporal processing may also be examined. Operators for dynamic magnetic field correction (Hahn et al., 2008, 2009), motion correction (Jenkinson et al., 2002), slice timing correction (Henson et al., 1999), temporal band-pass and notch filtering, and temporal smoothing (Gonzalez and Woods, 1992) may be developed by performing the Kronecker product with matrices other than identities. Thus, the full processing pipeline may be appropriately modeled with an extension to the described framework. In light of such a framework, statistical models may appropriately model the acquired data, rather than modeling data which has been preprocessed. Such models may allow scientists to statistically model the underlying physical changes associated with fcMRI and fMRI in more natural data (Rowe and Logan, 2004, 2005; Rowe, 2005), rather than modeling the observed indirect magnitude signal fluctuations.

Current computational limitations prevent the full implementation of such a statistical model. For a $96 \times 96$ $k$-space acquisitio matrix, the described operators are $18432 \times 18432$. If all double precision elements are saved to an array, such an array requires over 2.5 gigabytes of memory. In many cases, sparse matrix representations may be considered, but in cases including the Fourier operator or a modified Fourier operator, each element must be computed. As the matrix multiplication required to compute the alteration of a covariance matrix based upon the operation, $O\Gamma O^T = \sum$, requires three separate matrices in memory, $O$, $\Gamma$, and $\sum$, at least 7.5 gigabytes of memory must be addressed. Thus, 64-bit computing is essential. Further, hardware optimized matrix multiplication routines like the BLAS (Dongarra, 2002a,b), are essential for timely computations. If a time series of $N$ images were to be considered, the memory requirements would grow by a factor of $N^2$ and the time for calculations would likewise grow. As the number of computing cores in personal computers continues to grow, and the availability of memory continues to increase, such calculations for reasonable time series will likely become possible in the relatively near future.

In spite of these technological issues, this manuscript presents an exact theoretical means of computing image-space correlations which arise from processing operations, describes the construction of several common operators, presents theoretical results for common image acquisition techniques, and verifies those theoretical results in acquired echo planar data. The results illustrate that processing operations and physical processes affect computed voxel correlations, especially in local neighborhoods of voxels. This has strong implications for methods which consider correlations between nearby voxels, as the choice of processing techniques and the physical properties of the imaging subject may substantially affect computed results.


## Acknowledgements

This work was supported in part by NIH T32MH019992, R01EB000215 and R01EB007827.


## Appendix A. Magnitude squared covariance

Consider two magnitude squared variables

$$\begin{aligned} y_1 &= x_{1R}^2 + x_{1I}^2, \\ y_2 &= x_{2R}^2 + x_{2I}^2, \end{aligned} \quad (A.1)$$

where $x_{1R}$ and $x_{2R}$ are the real components of the first and second observations while $x_{1I}$ and $x_{2I}$ are the imaginary components. For the sake of this derivation, let:

$$\begin{array}{lll} E(x_{1R}) = \rho_1 \cos\theta_1, & \mathrm{var}(x_{1R}) = \sigma_{1R}^2 & \mathrm{cor}(x_{1R}, x_{2I}) = \Gamma_{RI}, \\ E(x_{1I}) = \rho_1 \sin\theta_1, & \mathrm{var}(x_{1I}) = \sigma_{1I}^2 & \mathrm{cor}(x_{1I}, x_{2I}) = \Gamma_{II}, \\ E(x_{2R}) = \rho_2 \cos\theta_2, & \mathrm{var}(x_{2R}) = \sigma_{2R}^2 & \mathrm{cor}(x_{1R}, x_{2R}) = \Gamma_{RR}, \\ E(x_{2I}) = \rho_2 \sin\theta_2, & \mathrm{var}(x_{2I}) = \sigma_{2I}^2 & \mathrm{cor}(x_{1I}, x_{2R}) = \Gamma_{IR}, \\ & & \mathrm{cor}(x_{1R}, x_{1I}) = \Gamma_1, \\ & & \mathrm{cor}(x_{2R}, x_{1I}) = \Gamma_2, \end{array} \quad (A.2)$$

where $\rho$ represents an observation's magnitude and $\theta$ represents an observation's phase. The magnitude and phase may be obtained from the reconstructed image. Note that the $\Gamma$ and variance values may be obtained from the complex correlation matrix.

The covariance between the magnitude squared variables assuming normally distributed noise is thus:

$$\begin{aligned} \mathrm{cov}(y_1, y_2) &= E(y_1 y_2) - E(y_1)E(y_2) \\ &= E(x_{1R}^2 x_{2R}^2) + E(x_{1R}^2 x_{2I}^2) + E(x_{1I}^2 x_{2R}^2) + E(x_{1I}^2 x_{2I}^2) - (E(x_{1R}^2) + E(x_{1I}^2))(E(x_{2R}^2) + E(x_{2I}^2)) \\ &= 2(\Gamma_{RR}^2 \sigma_{1R}^2 \sigma_{2R}^2 + \Gamma_{RI}^2 \sigma_{1R}^2 \sigma_{2I}^2 + \Gamma_{IR}^2 \sigma_{1I}^2 \sigma_{2R}^2 + \Gamma_{II}^2 \sigma_{1I}^2 \sigma_{2I}^2) + 4(\Gamma_{RR} \sigma_{1R} \sigma_{2R} \rho_1 \cos(\theta_1) \rho_2 \cos(\theta_2) \\ &\quad + \Gamma_{RI} \sigma_{1R} \sigma_{2I} \rho_1 \cos(\theta_1) \rho_2 \sin(\theta_2) + \Gamma_{IR} \sigma_{1I} \sigma_{2R} \rho_1 \sin(\theta_1) \rho_2 \cos(\theta_2) + \Gamma_{II} \sigma_{1I} \sigma_{2I} \rho_1 \sin(\theta_1) \rho_2 \sin(\theta_2)). \end{aligned} \quad (A.3)$$

By letting $x_1 = (x_{1R}, x_{1I})'$, $x_2 = (x_{2R}, x_{2I})'$, $E(x_1) = \mu_1$, $E(x_2) = \mu_2$, $\mathrm{cov}(x_1) = \sum_1$, $\mathrm{cov}(x_2) = \sum_2$, and $\mathrm{cov}(x_1, x_2) = \sum_{12}$, one can compactly write:

$$\begin{aligned} E(y_j) &= \mathrm{tr}(\Sigma_j) + \mu_j' \mu_j, & j = 1, 2, \\ \mathrm{var}(y_j) &= 2\mathrm{tr}(\Sigma_j' \Sigma_j) + 4\mu_j' \Sigma_j \mu_j, & j = 1, 2, \\ \mathrm{cov}(y_1, y_2) &= 2\mathrm{tr}(\Sigma_{12}' \Sigma_{12}) + 4\mu_1' \Sigma_{12} \mu_2, \end{aligned} \quad (A.4)$$

where $\mathrm{tr}(\cdot)$ denotes the trace operation.

## Appendix B. Fourier anomalies

The standard Fourier operator, $\Omega$, is described in Eq. (2). This operator may be modified to include anomalies in the Fourier encoding procedure, produced by $T_2^*$ decay and B-field inhomogeneity. Each anomaly introduces time dependent exponential

terms to the signal equation as shown in Eq. (6). The exponential terms for $T_2^*$ and $\Delta B$, denoted as $E(k_x, k_y, x, y)$, may be considered with their real and imaginary components through the Euler identity:

$$E(k_x, k_y, x, y) = e^{-t(k_x,k_y)/T_2^*(x,y)} e^{i\gamma\Delta B(x,y)t(k_x,k_y)} \tag{B.1}$$

$$E(k_x, k_y, x, y) = e^{-t(k_x,k_y)/T_2^*(x,y)} \cos(\gamma\Delta B(x,y)t(k_x,k_y)) + ie^{-t(k_x,k_y)/T_2^*(x,y)} \sin(\gamma\Delta B(x,y)t(k_x,k_y)). \tag{B.2}$$

These multiplicative terms may be included in the Fourier matrix with encoding anomalies as

$$\Omega_a = \Omega .* \begin{pmatrix} \Re(E(1,1,1,1)) & \cdots & \Re(E(m,n,1,1)) & -\Im(E(1,1,1,1)) & \cdots & -\Im(E(m,n,1,1)) \\ \vdots & \ddots & \vdots & \vdots & \ddots & \vdots \\ \Re(E(1,1,m,1)) & \cdots & \Re(E(m,n,m,1)) & -\Im(E(1,1,m,1)) & \cdots & -\Im(E(m,n,m,1)) \\ \Re(E(1,1,1,2)) & \cdots & \Re(E(m,n,1,2)) & -\Im(E(1,1,1,2)) & \cdots & -\Im(E(m,n,m,2)) \\ \vdots & \ddots & \vdots & \vdots & \ddots & \vdots \\ \Re(E(1,1,m,n)) & \cdots & \Re(E(m,n,m,n)) & -\Im(E(1,1,m,m)) & \cdots & -\Im(E(m,n,m,n)) \\ \Im(E(1,1,1,1)) & \cdots & \Im(E(m,n,1,1)) & \Re(E(1,1,1,1)) & \cdots & \Re(E(m,n,1,1)) \\ \vdots & \ddots & \vdots & \vdots & \ddots & \vdots \\ \Im(E(1,1,m,n)) & \cdots & \Im(E(m,n,m,n)) & \Re(E(1,1,m,n)) & \cdots & \Re(E(m,n,m,n)) \end{pmatrix}, \tag{B.3}$$

where .* indicates point-wise multiplication of the matrices. Clearly the form of $T_2^*$ and $\Delta B$ are dependent upon the physical system being imaged.

## Appendix C. Censoring and reordering acquired data

As acquired, the EPI *k*-space data is not in a format appropriate for the developed Fourier operators. Extra data must be censored, data acquired with negative frequency encoding gradients must be reversed, and the real data must be segregated from the imaginary data.

First, the extra points acquired during the phase encoding blips must be censored. A binary censoring matrix of dimension $2mn \times 2m(n+e)$ is used to multiply *S*. The censoring matrix is an identity matrix with the rows corresponding to the extra acquired points omitted. Mathematically, this can be described using the Kronecker product. Thus, the censoring matrix, *C*, is the Kronecker product of an identity matrix with a non-square matrix which includes an identity matrix and an $2n \times 2e$ matrix of zeros denoted by $Z(2n, 2e)$:

$$C = I_m \otimes [I_{2n}, Z(2n, 2e)]. \tag{C.1}$$

Thus, the extraneous points acquired during the phase encoding blips are removed through the use of the censoring matrix, $S_C = CS$. A toy example of a censoring matrix for an $8 \times 8$ array of *k*-space measurements with 1 point acquired during the phase encoding blips is shown in Fig. 1(d).

With the removal of the points acquired during the phase encoding blips, $S_C$ contains only the *k*-space observations that are on the *k*-space grid. The second step is to reorder the alternating lines where the data is collected with negative frequency encoding gradients. This is slightly more complicated than simply reversing the data as it is still in real–imaginary pairs which would be swapped to imaginary–real pairs if only row reversal was performed. Again, a Kronecker product is used to construct the row reversal operator, $\mathcal{R}$. To construct $\mathcal{R}$, a Kronecker product between $\mathcal{S}$, a "reverse identity" matrix, to reverse the row, and an identity matrix, to preserve the real–imaginary pairs, is used:

$$\mathcal{R} = \mathcal{S}_n \otimes I_2. \tag{C.2}$$

To apply this row reversal to only even lines, an alternating row reversal matrix, *R*, must be constructed. This is the Kronecker product between an identity matrix and a block, *B*, which preserves one row and reverses one row. Thus, the block is defined to be

$$B = \begin{pmatrix} I_{2n} & Z(2n, 2n) \\ Z(2n, 2n) & \mathcal{R} \end{pmatrix}, \tag{C.3}$$

and the alternating row reversal matrix is thusly

$$R = I_{m/2} \otimes B. \tag{C.4}$$

Note that this assumes an acquisition with reversed even rows, although an acquisition with reversed odd rows would require the trivial change of switching the positions of $I_{2n}$ and $\mathcal{R}$ in *B*. With the alternating row reversal matrix constructed, the alternating row reversal can be easily performed: $S_{RC} = RS_C$. A toy example of an alternating row reversal matrix for an $8 \times 8$ *k*-space data set is shown in Fig. 1(e).

The final step of converting *S* to *s* involves reordering $S_{RC}$ to include the real observations stacked above the imaginary observations. This operation is performed by a permutation matrix, $P_C$, which can be constructed by interleaving the columns of two non-square matrices. These matrices include $P_{C1} = [I_{mn}; Z(mn, mn)]$ and $P_{C2} = [Z(mn, mn); I_{mn}]$. The columns of these matrices are interleaved to produce $P_C$ by taking the first column of $P_{C1}$ followed by the first column of $P_{C2}$ and so on. This real–imaginary reordering can be performed through matrix multiplication to yield the data ordering required in Eq. (1), $s = P_C S_{RC}$. An example assuming an $8 \times 8$ *k*-space acquisition is shown in Fig. 1(f).

## Appendix D. Nyquist Ghost correction

Even and odd lines may be shifted in opposite directions to correct for the Nyquist ghost introduced from eddy current effects in EPI. This may be performed through the use of the Fourier shift theorem. The three operators which are described in this section reorder the data into sets of real and imaginary data for each row, Fourier transform each row, and apply a phase shift to the Fourier transformed row.

The permutation matrix is a binary matrix which can be constructed by interleaving blocks of columns of two non-square matrices to create a square matrix. The two matrices to be interleaved are $P_{R1} = [I_{mn}, Z(mn, mn)]$ and $P_{R2} = [Z(mn, mn), I_{mn}]$. The permutation matrix, $P_R$, results from taking the first n columns of $P_{R1}$ followed by the first *n* columns of $P_{R2}$, and so on. The signal is thus reordered to a column vector of the reals stacked above the imaginaries for each row through multiplication with $P_R$. As this is a permutation matrix, its inverse is simply its transpose. A graphical representation of $P_R$ for an $8 \times 8$ *k*-space acquisition is shown in Fig. 1(g).

The row Fourier transform matrix is the Kronecker product of an identity matrix with the Fourier transform matrix $\Omega_x$, as defined earlier, $\Omega_{row} = I_m \otimes \Omega_x$. A graphical representation of $\Omega_{row}$ for an $8 \times 8$ $k$-space acquisition is shown in Fig. 1(h).

The phase shift operator is the final necessary operator for performing a line shift. This operator multiplies the complex-valued Fourier transform of the line by a complex-valued exponential to implement the Fourier shift theorem. For a shift of $\phi$, the $j$th element of the row must be multiplied by $\exp(-i2\pi\phi j/n)$, or equivalently $\cos(2\pi\phi j/n) - i\sin(2\pi\phi j/n)$. Thus, the real component of the phase shifted $jth$ element is $\Re(f_j)\cos(2\pi\phi j/n) - \Im(f_j)\sin(2\pi\phi j/n)$, where $f_j$ is the $j$th element of the Fourier transformed row. Similarly, the imaginary component of the phase shifted $j$th element is $\Re(f_j)\sin(2\pi\phi j/n) + \Im(f_j)\cos(2\pi\phi j/n)$. Thus, for a row, this phase shift matrix operator is

$$\zeta = \begin{pmatrix} \cos(2\pi\phi 1/n) & \cdots & 0 & -\sin(2\pi\phi 1/n) & \cdots & 0 \\ \vdots & \ddots & \vdots & \vdots & \ddots & \vdots \\ 0 & \cdots & \cos(2\pi\phi n/n) & 0 & \cdots & -\sin(2\pi\phi n/n) \\ \sin(2\pi\phi 1/n) & \cdots & 0 & \cos(2\pi\phi 1/n) & \cdots & 0 \\ \vdots & \ddots & \vdots & \vdots & \ddots & \vdots \\ 0 & \cdots & \sin(2\pi\phi n/n) & 0 & \cdots & \cos(2\pi\phi n/n) \end{pmatrix}. \tag{D.1}$$

Shifting a row to the right by $\phi$ pixels is denoted by $\zeta^+$ while shifting a row to the left by $\phi$ pixels is denoted by $\zeta^-$. With this representation, the phase shifting of lines in alternating directions is denoted by $\Phi = I_{m/2} \otimes [\zeta^+, Z(2n, 2n); Z(2n, 2n), \zeta^-]$. A graphical representation of $\Phi$ with $\phi = 0.5$ and an $8 \times 8$ acquisition matrix is shown in Fig. 1(i).

## Appendix E. Partial Fourier interpolation

Conjugate symmetry ideally exists about the origin in $k$-space, as the reconstructed image is expected to be real-valued. This symmetry allows half of $k$-space to be generated without being acquired. Thus the acquired data array, $s$, only requires $2(m/2+1)n$ elements while the symmetrically generated data array, $s_S$, is $2mn$ elements. For the sake of consistency in notation, we assume that the remaining $2(m/2-1)n$ elements in $s$ are set to zero with the last $(m/2-1)n$ real observations being zero and the last $(m/2-1)n$ imaginary observations being zero. An equivalent symmetric $k$-space generation operator can be constructed which does not include these zero elements thereby reducing the operator size. However, in the considered case a square matrix, $H$, can be used for partial Fourier reconstruction. For the acquired real and imaginary points, the partial Fourier operator returns the observed values. For the generated point $(k_x, k_y)$, the partial Fourier operator returns the complex conjugate of the observed point at $(-k_x, -k_y)$. This partial Fourier operator multiplies the uncollected points by zero, so the values originally substituted into these points are irrelevant. The partial Fourier operator is thusly a $2mn \times 2mn$ matrix. This matrix which includes identity, $I$, "reverse identity," $\mathcal{S}$, and zero, $Z$, matrices is:

$$H = \begin{pmatrix} I_{(m/2+1)n} & Z((m/2+1)n, (m/2-1)n) & Z((m/2+1)n, mn) \\ Z((m/2-1)n, n) & \mathcal{S}_{(m/2-1)n} & Z((m/2-1)n, \frac{3}{2}mn) \\ Z((m/2-1)n, mn) & I_{(m/2+1)n} & Z((m/2+1)n, (m/2-1)n) \\ Z((m/2-1)n, (m+1)n) & -\mathcal{S}_{(m/2-1)n} & Z((m/2-1)n, \frac{m}{2}n) \end{pmatrix}. \tag{E.1}$$

A graphical representation of $H$ is shown in Fig. 1(j) for the case of an $8 \times 8$ symmetric $k$-space.

## Appendix F. Convolution

We will first describe the zero-filling operator, $F$, and then describe the apodization operator, $A$, which includes the typical Fermi apodization window and Gaussian smoothing window as specific cases. We will finally describe the image-space magnitude smoothing operator.

Zero-filling is often performed to yield an increase in apparent reconstructed resolution and to create an array which has dimensions of an integer power of two for fast Fourier transform routines (Gonzalez and Woods, 1992). In zero-filling, zeros are appended to the acquired $k$-space observations at higher spatial frequencies than are observed. It is well known that zero-filling is equivalent to image-space convolution with a sinc kernel. The zero-filling is done symmetrically to preserve the location of the $k$-space origin in the zero-filled array at $(m/2+1, n/2+1)$. The zero-filling matrix is a binary matrix containing blocks of zero and identity matrices. This parameterization of the zero-filling operator assumes that an even number of phase encode points, $P$, and an even number of frequency points, $J$, are to be added to the acquired data. The zero-filling operator is denoted as

$$F = I_2 \otimes \begin{pmatrix} F_P \\ I_m \otimes F_J \\ F_P \end{pmatrix} \tag{F.1}$$

where

$$F_P = Z\left(P/2, mn\right) \tag{F.2}$$

and

$$F_J = \begin{pmatrix} Z(J/2, n) \\ I_n \\ Z(J/2, n) \end{pmatrix}. \tag{F.3}$$

Thus, zeros are appended symmetrically around the acquired $k$-space matrix. It should be noted that this changes the dimensionality of $s$, and subsequent operators must be appropriately adjusted. An example of $F$ is shown in Fig. 1(k) for zero-filling a $4 \times 4$ $k$-space data set to an $8 \times 8$ data set.

Apodization and filtering can be considered with the Fourier convolution theorem, where convolution with a kernel in image-space is simply point-wise multiplication of the Fourier transform of the original kernel in $k$-space. Thus, any processing step which involves the point-wise multiplication of $k$-space observations with a kernel or the image-space convolution of the complex-valued image with a kernel can be considered with the apodization operator presented here. This apodization operator, $A$, is a diagonal matrix in which the non-zero elements correspond to the values of the $k$-space kernel for those points. If the values of the $k$-space kernel, $K$, are indexed across rows such that the first element of the first row is 1, the last element of the first row is $n$, the first element of the second row is $n+1$, and so on, the elements of $A$ are easily

defined such that $A_{j,j} = K(j)$. An example of $A$ is shown in Fig. 1(l) for the case of a simple $8 \times 8$ Hanning $k$-space window.

Explicit image smoothing is often performed on the reconstructed magnitude data. Such a process is different from smoothing the complex data (Lai et al., 1996) and is a non-linear process. However, with the magnitude squared covariance matrix known from the complex-valued covariance matrix, an operator, $S_{mm}$, may be developed to consider smoothing magnitude squared data. The first row of the operator consists of the kernel weights for each magnitude squared data point for the first smoothed magnitude squared data point. The second row includes the weights for the second point, and so on. An operator for smoothing an $8 \times 8$ data set with a Gaussian kernel with a three voxel FWHM is shown in Fig. 1(m). If image-space smoothing of the complex-valued data were preferred over $k$-space apodization, a complex-data smoothing operator, $S_m$ could be constructed as a block diagonal operator where the two diagonal blocks are filled with $S_{mm}$.

## References


Bernstein MA, King KF, Zhou XJ. Handbook of MRI pulse sequences. New York: Academic Press; 2004.

Birn RM, Diamond JB, Smith MA, Bandettini PA. Separating respiratory-variation-related fluctuations from neuronal-activity-related fluctuations in fMRI. NeuroImage 2006;31:1536–48.

Biswal BB, Yetkin FZ, Haughton VM, Hyde JS. Functional connectivity in the motor cortex of resting human brain using echo-planar MRI. Magnetic Resonance in Medicine 1995;34:537–41.

Dongarra J. Basic linear algebra subprograms technical forum standard. International Journal of High Performance Applications and Supercomputing 2002a;16:1–111.

Dongarra J. Basic linear algebra subprograms technical forum standard. International Journal of High Performance Applications and Supercomputing 2002b;16:115–99.

Friston KJ, Frith CD, Liddle PF, Frackowiak RS. Functional connectivity: the principle component analysis of large (PET) data sets. Journal of Cerebral Blood Flow and Metabolism 1993;13:5–14.

Glover GH, Li TQ, Ress D. Image-based method for retrospective correction of physiological motion effects in fMRI: RETROICOR. Magnetic Resonance in Medicine 2000;44:162–7.

Gonzalez RC, Woods RE. Digital image processing. Reading, MA, USA: Addison-Wesley Publishing Company; 1992.

Haacke EM, Brown R, Thompson M, Venkatesan R. Magnetic resonance imaging: physical principles and sequence design. New York, NY, USA: John Wiley and Sons; 1999.

Hahn AD, Nencka AS, Rowe DB. Dynamic compensation of $B_0$ field inhomogeneities restores complex fMRI time series activation power. In: Proceedings of the international society of magnetic resonance in medicine, vol. 16; 2008. p. 1251.

Hahn AD, Nencka AS, Rowe DB. Improving robustness and reliability of phase-sensitive fMRI analysis using temporal off-resonance alignment of single-echo timeseries (TOAST). NeuroImage 2009;44:742–52.

Henson RNA, Buchel C, Josephs O, Friston KJ. The slice-timing problem in event-related fMRI. NeuroImage 1999;9:125.

Jenkinson M, Bannister PR, Brady JM, Smith SM. Improved optimisation for the robust and accurate linear registration and motion correction of brain images. NeuroImage 2002;17:825–41.

Jesmanowicz A, Bandettini PA, Hyde JS. Single-shot half k-space high-resolution gradient-recalled EPI for fMRI at 3 Tesla. Magnetic Resonance in Medicine 1998;40:754–62.

Jesmanowicz A, Wong EC, Hyde JS. Phase correction for EPI using internal reference lines. In: Proceedings of the society of magnetic resonance in medicine, vol. 12; 1993. p. 1239.

Jezzard P, Balaban RS. Correction for geometric distortion in echo planar images from $B_0$ field variations. Magnetic Resonance in Medicine 1995;34:65–73.

Kriegeskorte N, Bodurka NJ, Bandettini PA. Artifactual time course correlations in echo-planar fMRI with implications for studies of brain function. International Journal of Imaging Systems and Technology 2008;18:5–6.

Lai S, Reichenbach JR, Haacke EM. Commutator filter: a novel technique for the identification of structures producing significant susceptibility inhomogeneities and its application to functional MRI. Magnetic Resonance in Medicine 1996;36:781–7.

Nencka AS, Hahn AD, Rowe DB. The use of three navigator echoes in Cartisian EPI reconstruction reduces Nyquist ghosting. In: Proceedings of the international society of magnetic resonance in medicine, vol. 16; 2008. p. 3032.

Nencka AS, Rowe DB. Image space correlations induced by k-space processes. In: Proceedings of the organization for human brain mapping, vol. 13; 2007.

Nencka AS, Rowe DB. Apodization and smoothing alter voxel time series correlations. In: Proceedings of the international society of magnetic resonance in medicine, vol. 16; 2008. p. 2457.

Pfeuffer J, Van de Moortele PF, Ugurbil K, Hu X, Glover GH. Correction of physiologically induced global off-resonance effects in dynamic echo-planar and spiral functional imaging. Magnetic Resonance in Medicine 2002;47:344–53.

Rowe DB. Modeling both the magnitude and phase of complex-valued fMRI data. NeuroImage 2005;25:1310–24.

Rowe DB, Logan BR. A complex way to compute fMRI activation. NeuroImage 2004;23:1078–92.

Rowe DB, Logan BR. Complex fMRI analysis with unrestricted phase is equivalent to a magnitude-only model. NeuroImage 2005;24:603–6.

Rowe DB, Nencka AS, Hoffmann RG. Signal and noise of Fourier reconstructed fMRI data. Journal of Neuroscience Methods 2007;159:361–9.

Shmueli K, van Gelderen P, de Zward JA, Horovitz SG, Fukunaga M, Jansma JM, et al. Low frequency fluctuations in the cardiac rate as a source of variance in the resting state fMRI BOLD signal. NeuroImage 2007;38:306–20.

van de Ven VG, Formisano E, Prvulovic D, Roeder CH, Linden DEJ. Functional connectivity as revealed by spatial independent component analysis of fMRI measurements during rest. Human Brain Mapping 2004;22:165–78.